APL Photonics

RESEARCH ARTICLE | DECEMBER 29 2025

# High-flux single-photon LiDAR imaging through obscurants at count rates above pile-up limitations

**Special Collection:** Single-photon detectors: new physical principles, circuits and applications

Serena Farina ✉ ; Aurora Maccarone ; Ivan Labanca ; Aongus McCarthy ; Giulia Acconcia ;
Ivan Rech ; Gerald S. Buller

*APL Photonics* 10, 126122 (2025)
https://doi.org/10.1063/5.0301407

AIP Publishing

APL Photonics ARTICLE pubs.aip.org/aip/app

# High-flux single-photon LiDAR imaging through obscurants at count rates above pile-up limitations

**Cite as:** APL Photon. 10, 126122 (2025); doi: 10.1063/5.0301407
**Submitted:** 8 September 2025 • **Accepted:** 10 December 2025 •
**Published Online:** 29 December 2025

**Serena Farina,**[1,a)] **Aurora Maccarone,**[2] **Ivan Labanca,**[1] **Aongus McCarthy,**[2] **Giulia Acconcia,**[1] **Ivan Rech,**[1] **and Gerald S. Buller**[2]

## AFFILIATIONS

[1] Politecnico di Milano, Dipartimento di Elettronica, Informazione e Bioingegneria, Piazza Leonardo Da Vinci 32, 20133 Milan, Italy
[2] Institute of Photonics and Quantum Sciences, and Scottish Universities Physics Alliance (SUPA), Heriot-Watt University, Edinburgh EH14 4AS, United Kingdom

**Note:** This paper is part of the Special Topic on Single-photon detectors: new physical principles, circuits and applications.
[a)] **Also at:** INAF-Istituto di Astrofisica Spaziale e Fisica Cosmica, Via Alfonso Corti 12, 20133 Milano, Italy and Scuola Universitaria Superiore IUSS Pavia, Piazza della Vittoria 15, I-27100 Pavia, Italy.
**Author to whom correspondence should be addressed:** serena.farina@polimi.it

## ABSTRACT

Light detection and ranging (LiDAR) represents a widely used method to obtain highly detailed three-dimensional maps of the environment. While LiDAR generally benefits from a high-flux operation regime, the use of the time-correlated single-photon counting (TCSPC) technique can be limited by the pile-up phenomenon, which prevents acquisition rates higher than 5% of the laser excitation rate. If higher acquisition rates are used, pile-up can affect the timing data by introducing distortions in the histogram. Here, we analyze and discuss these strong distortion effects induced by pile-up in the specific case when measuring low-reflectivity targets through obscurants, both for single-point measurements and three-dimensional imaging. Furthermore, we demonstrate that it is feasible to overcome the enforced constraint, reaching a count rate of almost 30% (an order of magnitude higher) without notable distortion, even in the presence of complex multi-echo waveforms. This is accomplished through a purely hardware-based solution, by means of a precise matching between the single-photon detector dead time and the laser period. The achieved results pave the way to faster single-photon LiDAR in multiple applications, such as imaging through obscurants, underwater imaging, and hyperspectral and multispectral imaging.

## I. INTRODUCTION

Nowadays, the light detection and ranging (LiDAR) technique[1] is used as a means of three-dimensional imaging in a variety of fields, including autonomous driving[2,3] and remote or harsh environment exploration.[4–8] Direct time-of-flight LiDAR uses pulsed laser illumination, where the scattered return optical signal from the target is timed with respect to the outgoing laser pulse. By measuring the round trip time, the distance to the target can be calculated. In particular, single-photon LiDAR has emerged in recent years as a potential LiDAR candidate due to its improved surface-to-surface resolution and higher levels of optical detectivity. Hence, this technique has the potential to perform at longer ranges, typically well within laser eye-safety thresholds.[9] Single-photon LiDAR generally utilizes the time-correlated single photon counting (TCSPC) method,[10] where sub-nanosecond temporal precision is routinely used.[11,12] Unfortunately, TCSPC can be limited by the pile-up phenomenon, where statistical distortion in the timing histogram occurs when the event acquisition rate is higher than ~5% of the laser pulse rate, due to the dead times masking the arrival of the latest photons.[10] For this reason, it is preferable to operate a LiDAR system at an acquisition rate in the range of 1%–5% of the laser frequency, thus making TCSPC a slow detection technique. This is clearly in contrast with the high photon-flux regime that would be desirable in those LiDAR measurements where low-reflectivity targets are behind or inside highly scattering media.[5,13–15] For instance, this includes imaging through obscurants,[13] underwater and fog imaging,[4,15] and hyperspectral and multispectral imaging.[16–18] In these situations, the interposed medium is likely to absorb or scatter most of the incoming light, strongly attenuating the return signal from the object being imaged, and therefore a higher incident laser power would be required.[4] However, this would result in a higher return from the media, significantly increasing the detected photon count rate and resulting in pile-up distortions of the histogram. It is worth mentioning that, in those cases, not only the single-target return but also the full LiDAR waveform is of interest for data analysis.

In order to surpass the pile-up limitation in LiDAR, different approaches have been presented so far in the scientific literature for single-peak histograms, and a major distinction needs to be made between software and hardware solutions. The former are extremely convenient from a practical standpoint, since they can be simply applied during the post-processing phase; yet, they require the development of highly specific statistical models to describe pile-up. Instead, the hardware approaches rely on architectural modifications to be effective, and therefore require a substantial effort in terms of time during the system design phase. The simplest software correction algorithms are based on the classic pile-up model, meaning that the acquisition is synchronous to the laser period, and only one photon per period can be detected. The first correction algorithm leveraging this model was reported by Coates in Ref. 19 for fluorescence, followed by more recent LiDAR works by Heide *et al.*[20] and Tontini *et al.*[21] These models correctly describe the historical timing electronics with single-hit capability, but they do not take into account the possible multiple sources of dead time that are present in modern TCSPC systems.[22] To include the current dominant pile-up sources, i.e., the dead times of the detector and of the TCSPC timing electronics, in Ref. 23. Isbaner *et al.* proposed a new iterative algorithm for dead time correction, and in Refs. 24 and 25, Rapp *et al.* presented a novel statistical model based on a Markov chain. Moreover, in Ref. 26, Incoronato *et al.* also considered the pile-up effects deriving from a limited memory availability on the detector chip. Regarding instead the hardware solutions, the current research is leading toward a reduced dead time for single-photon detectors,[27–29] and toward highly parallel systems composed of multiple replicated channels,[22,30] which can both mitigate the rising of pile-up effects. In parallel, Gupta *et al.* proposed the usage of a pixel-wise adaptive attenuation to achieve an optimum flux for each pixel,[31] or the adoption of an asynchronous time gating technique;[32] Tontini *et al.*[33] proposed instead the on-chip linearization of the detector response, allowing to directly extract the time-of-flight information without the need of a full histogram. Finally, the electronics dead time today being almost negligible with respect to the typical photon count rate,[34,35] some novel approaches primarily address the effects of detector dead time, as the hardware method proposed by Cominelli *et al.* in Ref. 36 and the software solution proposed by Rech *et al.* in Ref. 37.

In this complex scenario, the aim of this paper is twofold. On the one hand, we propose a detailed investigation of the pile-up phenomenon in LiDAR-based single-photon depth imaging through obscurants. To the best of our knowledge, this analysis has not yet been presented elsewhere, but can be extremely beneficial for scientists to understand and recognize the typical pile-up features in single-photon LiDAR measurements. On the other hand, we propose for the first time the application to LiDAR of a hardware-based pile-up free acquisition methodology (based on the theory of Cominelli *et al.*[36]), which can eliminate distortions directly at measurement time by matching the detector dead time to the laser period, without any further need of post-processing. Compared to the current hardware solutions, this approach involves only a single channel with consequent benefits in terms of electronics and optics complexity. Unlike the current software methods, this solution allows for a truly real-time measurement, no histogram correction being needed after acquisition. However, to date, the method has been successfully simulated and demonstrated only for mono-exponential fluorescence decays in the biological field,[38] but never yet applied to multi-echo LiDAR waveforms. The effects and details of the same method applied to multi-echo LiDAR are not obvious, as the recorded waveforms exhibit in the two cases peculiar characteristics that require different approaches for data interpretation and processing. Consequently, the presented experimental measurements involve an in-depth analysis of both single-point measurements, to clearly observe the multi-echo histogram with obscurants and complete depth images. In both situations, the pile-up distortion is totally removed by applying the proposed technique, and the full acquired waveform is restored, thus paving the way to fast single-photon LiDAR in multiple applications.

The remainder of the paper is organized as follows: in Sec. II, the adopted pile-up free method is presented and the experimental setup is described; in Sec. III, the results of single-point measurements and of imaging experiments are reported; finally, in Sec. IV, the obtained results are discussed and compared to other methods, and in Sec. V, conclusions are drawn.

## II. METHODS

### A. Pile-up free acquisition

As mentioned above and also clarified in scientific literature, different sources of dead time may affect a TCSPC experiment.[22] Today, the main sources for a commercial non-integrated system consist of the detector and the timing electronics dead times, which can closely interact giving rise to complex pile-up distortions as shown in Refs. 23 and 25. To simplify the pile-up management, the most straightforward solution is to completely avoid at least one of the two effects: for this reason, we decided to employ a fast timing module, featuring an electronics dead time much lower than that of a typical detector. To this aim, different commercial options are available on the market, such as the MultiHarp 150 from PicoQuant[34] or the Time Tagger Ultra from Swabian Instruments.[39] For this experiment, we selected instead a prototype module that was already available in our laboratories, with a maximum average count rate of 80 Mcps, multi-hit capabilities, and a full-scale range (FSR) selectable among 12.5, 25, 50, and 100 ns.[40] Being the possible laser rate for the ranging experiments from 10 to 40 MHz, the introduced electronics dead time is negligible with respect to the achievable photon count rates in these measurements.

Regarding instead the detector dead time, we applied a methodology that has been theoretically proposed by Cominelli *et al.* in

Ref. 36 for free-running single-photon avalanche diodes (SPADs). This technique is based on a precise time matching between the detector dead time and the laser period, which means that the detector becomes completely blind for an entire laser period, each time a photon is detected. In this way, a complete period is omitted from the measurement and the statistics of the input light signal is not altered. This method has been successfully applied with simple mono-exponential decays in fluorescence lifetime measurements,[38] but no results are reported in the literature regarding LiDAR measurements.

As the typical LiDAR signal, i.e., a Gaussian peak, is extremely different from the exponential ones in fluorescence experiments, preliminary numerical simulations have been performed to predict possible pile-up effects on the full LiDAR waveform, and to compare them with experimental results. In fact, while in fluorescence imaging, we expect a variation of lifetime as a consequence of pile-up, in LiDAR, we observe a more widespread effect on the full waveform.[24] Similar to what is reported in Ref. 36, the simulations are based on three steps: (i) the random extraction of photons from a periodical light waveform, consisting in this case of a sequence of Gaussian peaks; (ii) the emulation of the detector behavior in terms of dead time; and (iii) the collection and accumulation of the recorded photons into the final histogram. Further details on pile-up simulations can be found in the supplementary material. The most significant findings are reported in Figs. 1 and 2, where the simulations are executed for a laser repetition rate of 10 MHz over a FSR of 100 ns with a time bin of 6.1 ps, to be consistent with the lowest possible laser repetition rate and the timing module. In Fig. 1, a single Gaussian peak with a full-width at half-maximum (FWHM) of 300 ps and an input signal-to-background ratio (SBR)[41] of $10^3$ is shown: on the left, a low rate curve with an average number of impinging photons per period $P_{imp}$ equal to 0.05 is shown, along with the same curve at high rate ($P_{imp} = 1$) with a matched dead time of 100 ns. The low rate curve is reported for a generic dead time, being the shape of the curve not affected by the employed dead time, as predicted by theory.[10] On the right, the curves are instead simulated for the same high count rate

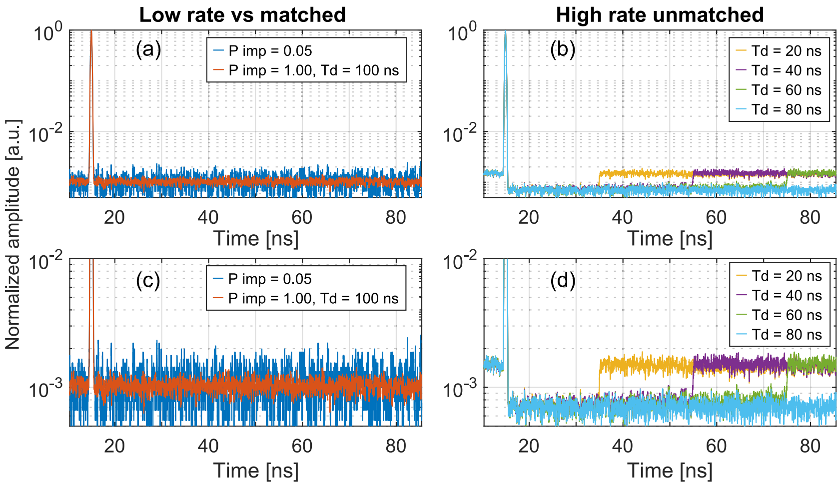

**FIG. 1.** Simulation of a single Gaussian peak with a FWHM of 300 ps over a FSR of 100 ns with an input SBR of $10^3$. All curves are simulated with the same number of photons ($800 \times 10^3$) and normalized with respect to the peak. Full Gaussian peak on top and corresponding zoom on the region of interest at the bottom. (a) and (c) Low rate curves ($P_{imp}$ = 0.05) compared to high-rate curves ($P_{imp}$ = 1) with matched dead time. (b) and (d) High-rate curves with unmatched dead times, showing an artificial hole in the background.

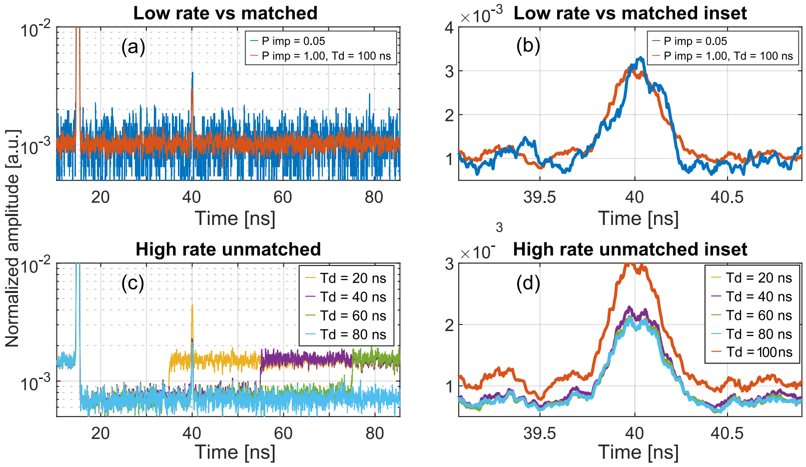

**FIG. 2.** Simulation of two Gaussian peaks with a FWHM of 300 ps over a FSR of 100 ns with an input SBR of $10^3$ and a PPR of 500. All curves are simulated with the same number of photons ($2 \times 10^6$) and normalized with respect to the peak. (a) Low rate curve ($P_{imp}$ = 0.05) compared to high-rate curve ($P_{imp}$ = 1) with matched dead time. Only the region of interest (baseline) is shown. (b) Zoom on the second peak from (a) on a linear scale. (c) High-rate curves with unmatched dead times, showing an artificial hole in the background. Only the region of interest (baseline) is shown. (d) Zoom on the second peak from (c) on a linear scale, showing a reduction of the peak amplitude at unmatched dead times due to pile-up.

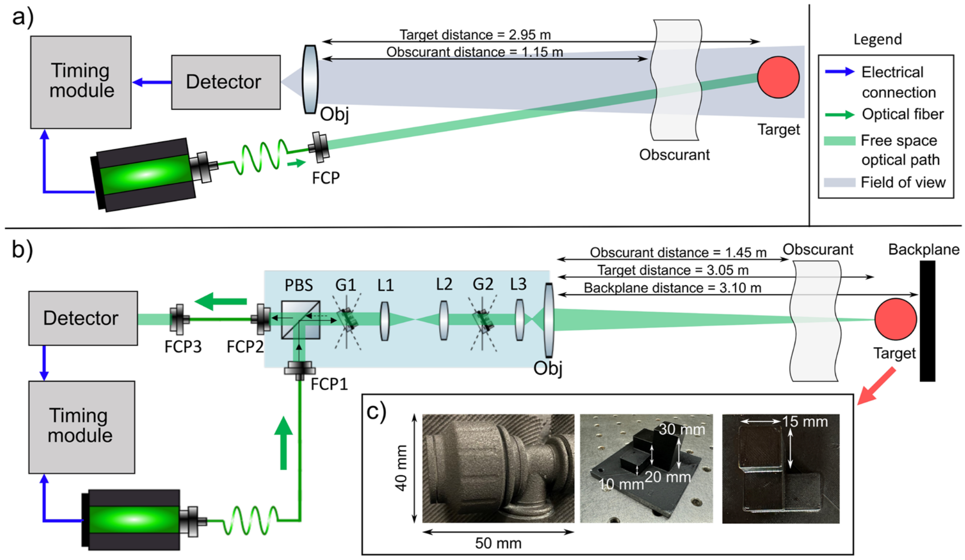

**FIG. 3.** Schematic diagram of the experimental setup used to investigate pile-up effects in LiDAR. (a) Bistatic configuration with separated transmit and receive light paths. (b) Monostatic configuration, where the outgoing and return paths are coaxial. PBS: polarizing beam splitter, FCP: fiber collimation package, L: lens, G: galvanometer mirror, Obj: objective. (c) Photograph and dimensions of the two employed targets: a plastic pipe joint and a 3D printed object containing three pillars with square cross-sections.

with unmatched dead times from 20 to 80 ns. While the matched dead time curve is in accordance with the reference one at low rate, the other curves on the right show a remarkable distortion, especially in the background with an artificial hole that lasts for the whole duration of the dead time. Compared to exponential signals,[36,38] the distortion observed here is clearly different, for the reason that all the photons belonging to the Gaussian signal are concentrated in a reduced time span. Since the introduced pile-up distortion is proportional to the signal area, a shift in the background is observed for the Gaussian shape, being instead not present for the exponential case. In Fig. 2, the same type of simulation is replicated by using two Gaussian peaks with a peak-to-peak ratio (PPR) of 500, representing a typical situation for a LiDAR measurement through obscurants. The same distortion phenomena of the previous figure appear visible also here, with the additional effect of a reduction in the target peak amplitude in case of pile-up as can be observed in the image zooms on the right.

In order to experimentally replicate the simulations and to thoroughly investigate the impact of pile-up on depth imaging, we employed the detection module proposed in Ref. 40, which allows controlling the dead time of a SPAD with a high precision, thanks to a tunable active-quenching circuit (AQC).[42] It is worth mentioning that detector non-idealities (e.g., dead time jitter or reset time) do not alter the possibility of applying the technique, as already demonstrated in Refs. 36 and 40. Deterministic variations of dead time may instead alter the obtained results, and for this reason, proper calibration procedures should be devised, as in Ref. 43. A full discussion on practical details of dead time matching is provided in the supplementary material. The selected module contains a 50-μm diameter custom-technology thin-junction SPAD[44] featuring a dark count rate of 16.5 kcps at 27 °C and an afterpulsing probability of 5%.[45] This module and the previously mentioned timing module were integrated in the overall optical setup to implement a fully automatized acquisition procedure.

### B. Experimental setup

Two different optical transceiver configurations have been employed to obtain the experimental data: (i) a bistatic transceiver system and (ii) a custom-designed monostatic scanning transceiver [schematically shown in Figs. 3(a) and 3(b), respectively]. The former is characterized by two distinct optical paths for the forward light toward the target and for the backward light reflected by the target, avoiding the detection of potential reflections from optical elements within the transceiver system. Hence, this configuration was used to investigate histogram distortions when only two return peaks were detected, one peak corresponding to an obscurant material and the other corresponding to the target. Conversely, the monostatic transceiver featured a coaxial path for the two opposite-traveling light channels, with the disadvantage of a high number of internal backreflections generated by the surface of the optical components common to the receive and transmit channels. This optical configuration was used to investigate waveforms with several detection peaks. Both configurations were employed in single-point measurements, while only the monostatic transceiver was leveraged for depth imaging experiments. For both setups, the light source consisted of a picosecond pulsed laser (VisUV, by PicoQuant), emitting in the green ($\lambda$ = 532 nm, pulse width = 90 ps FWHM) at a repetition rate of 20 MHz. The imaged targets [shown in Fig. 3(c)] were placed behind an obscurant tissue, with a measured transmittance of 35%. A detailed explanation of the setup is reported in the supplementary material.

## III. EXPERIMENTAL RESULTS

In order to gain a clear insight on pile-up effects over LiDAR experiments through obscurants, the measurements were organized in two successive steps. First, we performed single-point acquisitions with both the bistatic and the monostatic transceivers at different dead times. In fact, a single-point experiment guarantees a higher SBR, thanks to a longer integration time, which is typically not compatible with scanning protocols due to time constraints. Successively, we dealt with depth imaging, by using two different targets: a 3D printed pillar target with known depth features and a pipe target to observe a more complex shape [Fig. 3(c)]. The whole measurement procedures and the achieved results are presented and discussed in the next sections. More precisely, while in the literature, pile-up is mostly considered as responsible of peak displacement[20,25] in LiDAR, in the remainder of the paper, we highlight other macroscopic effects that can cause additional or missing feature identification, especially in full-waveform analysis.[8]

## A. Single-point measurements

For the single-point acquisitions, a low-reflectivity flat target was placed behind a semi-transparent obscurant (a lens-cleaning tissue), with a distance between the two on the order of 1.6 and 1.8 m for the bistatic and monostatic configurations, respectively. The acquisition time per waveform was set to 50 s, with a total number of recorded photons of 10 Mcounts in case of a low photon rate ($P_{rec} = 0.01$) and 250 Mcounts in case of the highest rate ($P_{rec} = 0.25$). It is worth mentioning that in a practical experiment, the average number of photons impinging on the detector per each period ($P_{imp}$) is not directly measurable, and therefore all the subsequent measurements refer to the actual average number of photons recorded by the detector per period ($P_{rec}$). The relation between these two quantities is better clarified in Refs. 36 and 38.

### 1. Bistatic configuration

In Table I, the acquisition parameters used with the bistatic configuration are summarized, including three different measurement sets, where the optical power was set in order to achieve the desired count rates for different optical components within the same configuration.

In order to investigate the pile-up effect, in the first measurement set, the dead time of the detector has been swept from almost 13–80 ns, by acting on the analog control voltage $V_Q$ of the AQC that modifies the hold-off time applied to the SPAD.[42] The achieved results are shown in Fig. 4 as a function of the applied dead time and $V_Q$ values, with the acquired curves normalized with respect to the baseline, for a more effective visualization of pile-up in case of different SBRs. The top left graph shows the full-scale histogram, while the other graphs are cropped as to better appreciate the region of interest. As can be observed, each graph shows the presence of two peaks, one corresponding to the tissue and the second one corresponding to the target behind. However, it appears evident that for low-rate curves, the target peak is totally hidden by the noise, while for high-rate curves, the peak is clearly distinguishable over the background. For such a reason, the usage of a high optical flux constitutes here the preferred solution, especially in the case of LiDAR with low-reflectivity targets.

In agreement to what predicted by simulations, the first and higher peak results are almost undistorted, while an intensity reduction is observed just after, extending for a time span equal to the detector dead time, and causing therefore the downshift of both the baseline and the target peak. As a result of the selected FSR of the timing module being set equal to the laser period (50 ns), the baseline downshift is periodical and it wraps around the laser period, as already shown in Refs. 36 and 38 and visible for a dead time of 80 ns. At the end of the dead time, the baseline recovers its original value, but differently from the simulation, an unexpected exponential decay is present. Being this feature also visible on low-rate curves, it cannot be attributed to any pile-up effects, but rather to a well-known SPAD non-ideality, i.e., the afterpulsing.[45,46] This phenomenon consists in the generation of a correlated detector count in the absence of an actual photon in the time interval following a photon detection, due to the release of carriers previously trapped in silicon defects. As a further confirmation of the hypothesis, the phenomenon decreases its magnitude with increasing dead times, following the typical trends of the detector afterpulsing. Finally, as expected from simulations, with a matched dead time of 50 ns, the baseline shift induced by pile-up is effectively removed, as can be seen in Fig. 4(b) on the left. In this case, the onset of afterpulsing is situated in correspondence of the obscurant peak. In particular, the afterpulsing appears to be different at high and low count rates,

**TABLE I.** Acquisition parameters for single-point bistatic and monostatic measurements. $P_{rec}$ represents the average number of photons recorded by the detector per period.

| Set number | $\mathbf{P_{rec}}$ (counts) | Rate (Mcps) | Dead time (ns) | Opt. power ($\mu$W) | Env. light |
|---|---|---|---|---|---|
| | | | Bistatic configuration | | |
| 1 | 0.01 | 0.2 | ~13–80 | 0.38 | No |
| | 0.25 | 5 | ~13–80 | 27 | No |
| 2 | 0.01 | 0.2 | 80 | 26 | No |
| | 0.25 | 5 | 23; 50 | 2600 | No |
| 3 | 0.01 | 0.2 | ~13–80 | 0.38 | Yes |
| | 0.25 | 5 | ~13–80 | 27 | Yes |
| | | | Monostatic configuration | | |
| 1 | 0.02 | 0.4 | 80 | 1306 | No |
| | 0.25 | 5 | ~13–50 | 9000 | No |

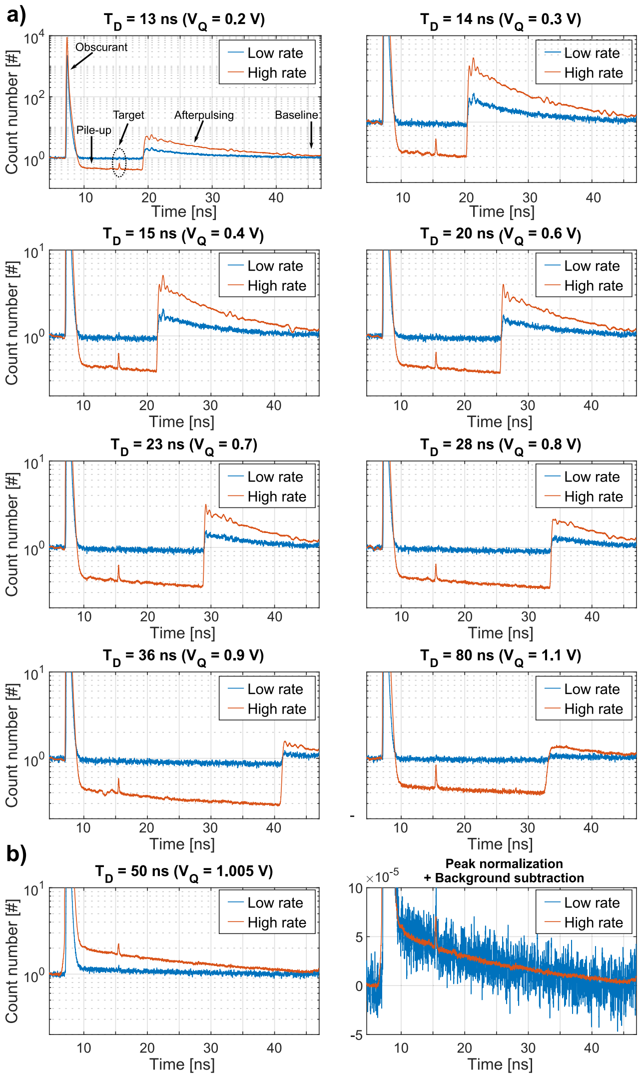

**FIG. 4.** (a) Acquired waveforms at low and high rates with the bistatic setup at different unmatched dead times from 13 to 80 ns (i.e., at different $V_Q$ voltages from 0.2 to 1.1 V), featuring both the tissue and the target peaks. The top left curves are entirely shown, while the others are cropped over the region of interest. (b) Acquired waveforms with a matched dead time of 50 ns ($V_Q$ = 1.005 V). No pile-up distortion is observed in this situation. Left: Curves with baseline normalization. Right: Zoom on the same curves with normalization at peak and background subtraction.

but this represents only a visual effect given by baseline normalization in case of different SBRs. In fact, since the low rate and high rate curves are acquired with the same background, but with different laser powers, the SBR is not the same for the two curves. To clarify this point, Fig. 4(b) on the right reports the same curves with background subtracted and normalized with respect to the peak, in such a way to exclude the effect of the different SBRs. The obtained curves appear to be overlapped, thus demonstrating that the shape of the waveform is preserved between the low-rate acquisition and the high-rate one in case of matched dead time. This represents, in our opinion, a clear proof of the potential of the applied technique to radically solve pile-up related issues also in LiDAR measurements.

Besides baseline displacement, a second important effect of pile-up over multi-echo waveforms has been observed during the first set of measurement, and more precisely the presence of a blind spot for specific dead time values, or equivalently for specific spatial positions of the target. In particular, a reduced set of dead time values from 57 to 61 ns have been applied in order to observe the transitioning of the dead time step in correspondence of the target peak. Such cases are illustrated in Fig. 5, where the orange curves acquired with the mentioned dead time values are compared toward the blue curve at the longest dead time (80 ns). As can be seen, the target peak completely disappears for a dead time of 58.3 ns and is partially overlapped for a larger dead time interval. The situation is made worse by the presence of ringings, which are generated due to bias voltage oscillations after detector reset. As a practical consequence, any target object situated in the histogram at a distance from the obscurant peak equal to the dead time is missed, giving therefore rise to a blind spot in the generated depth maps. This clearly represents a major limitation for LiDAR acquisitions, which cannot be simply overcome with a pure software correction, but requires for a hardware solution, such as the one proposed here.

After identifying the possible distortions affecting multi-echo waveforms due to pile-up, a second set of measurements (see Table I) was acquired, with the aim of quantifying the target peak reduction. Indeed, in the first set of measurements, the target peak was almost

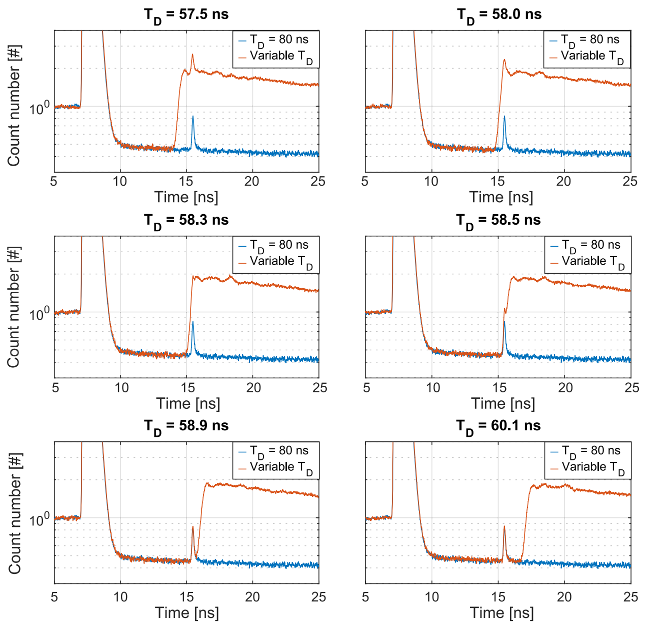

**FIG. 5.** Acquired waveforms in orange at high rates with the bistatic setup at different dead times from 57 to 60 ns, in correspondence of the end of the dead time. The blue curve represents the same waveform with the maximum dead time of 80 ns for comparison. The target peak completely disappears for a dead time of 58.3 ns generating a blind spot.

invisible at low rates, and a precise quantification of its amplitude would therefore be unreliable. The obtained results are reported in Fig. 6, where a higher return from the target was acquired thanks to a reduced thickness of the interposed tissue. As a figure of merit, the ratio $\mathscr{R}$ between the target peak and the obscurant peak after baseline subtraction was considered, which can be expressed as follows:

$$\mathscr{R} = \frac{(A_t - B_t)}{(A_o - B_o)}, \tag{1}$$

where $A_t$ and $A_o$ represent the amplitude of the target and obscurant peaks, respectively, and $B_t$ and $B_o$ represent the local baseline before the peaks. By referring to the low rate curve, the $\mathscr{R}$ value results equal to 0.0054, and a similar result holds for the high-rate curve with a matched dead time of 50 ns. Conversely, for the high-rate curve with unmatched dead time (23 ns), the $\mathscr{R}$ value is wrongly decreased to 0.0043 (20% less). Since in this case, the pile-up distortion is mainly introduced by the obscurant peak, the reduction in the recording probability affects equally the target amplitude $A_t$ and the local baseline $B_t$, thus decreasing the overall $\mathscr{R}$ parameter. Unfortunately, the presence of such error bears a strong impact on those measurements, where the reflectivity of objects shall be estimated through LiDAR measurements, such as in multispectral and hyperspectral LiDAR.[16–18]

All measurements were performed in dark laboratory conditions; hence, a last set of measurements (see Table I) was acquired to observe possible differences in case of strong ambient light (1.2 Mcps on the detector), being this the typical situation of a practical LiDAR experiment. For the sake of compactness, the results of this last set are not reported in the paper, but the main features and arguments of the previous discussions still apply here, with the sole difference of a reduced afterpulsing due to the dominant background effect. In conclusion, it is possible to state that the usage of the proposed hardware pile-up free method is practically feasible and advantageous also in case of different environmental conditions.

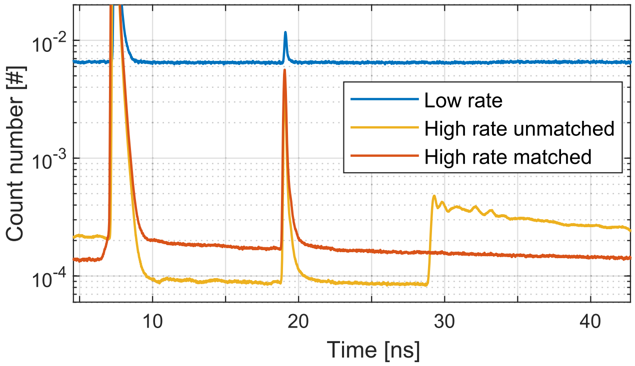

FIG. 6. Acquired waveforms with the bistatic setup at low rate and high rates with matched (50 ns) and unmatched (23 ns) dead times, with a target peak visible also for low rates. The curves are normalized with respect to their peak, showing thus different SBRs. Only the region of interest (baseline) is shown. The curve with unmatched dead time is affected by a proportional reduction of both the target peak amplitude and the baseline.

### 2. Monostatic configuration

Given the promising results achieved thanks to the usage of the pile-up free method with the bistatic setup, we decided to perform measurements with the monostatic transceiver to investigate the case of several peaks in the histogram. The monostatic configuration is often used for LiDAR depth imaging,[4,13,47] as the receive and transmit channels are coaxial, and therefore do not require realignment for different target distances. The employed experimental parameters almost follow the ones of the bistatic configuration, and are reported in Table I. Figure 7 illustrates instead the acquired waveforms, with the top left curves completely shown and the others cropped to the region of interest. As can be observed, three different peaks are present in the graph: a first irregular peak, which was not present with the bistatic setup, followed by the tissue and the target peaks. The first peak is generated by undesired internal reflections through the optical elements of the monostatic transceiver,[47] whose remarkable amplitude typically affects the acquisition of the actual targets outside the optical system. In this case, both the internal reflections and the tissue peaks may give rise to pile-up, depending on their relative intensity ratio; moreover, both of them generate an

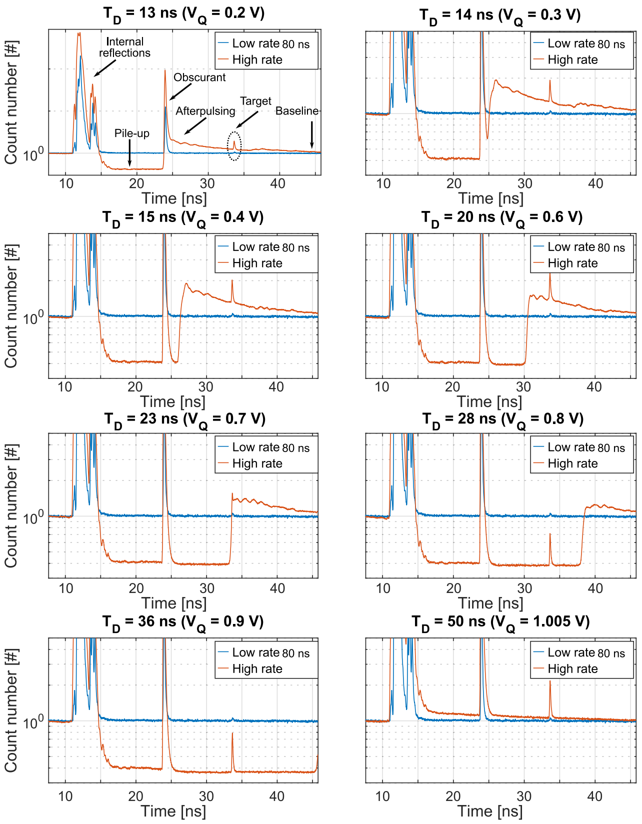

FIG. 7. Acquired waveforms with the monostatic setup at low rate with a dead time of 80 ns and at high rates at different dead times from 13 to 50 ns (i.e., at different $V_Q$ voltages from 0.2 to 1.005 V), featuring the internal reflections, the tissue, and the target peaks. The top left curves are entirely shown, while the others are cropped over the region of interest. No pile-up distortion is observed with a matched dead time of 50 ns ($V_Q = 1.005$ V).

afterpulsing decay, as can be clearly seen for a dead time of 14 ns. Regarding pile-up, the same considerations apply as for the bistatic measurements, but with the additional issue that two different conditions can arise: (i) both the tissue and the target are affected by baseline shift, as for example, with a dead time of 28 ns or (ii) only the tissue peak is affected by a baseline shift, as for example, with a dead time of 20 ns. Clearly, this second situation makes it challenging to correctly estimate the number of photons in the return peak from the target. Furthermore, it is worth noting that the blind spot issue is still present, this time for a dead time of almost 23 ns.

In order to avoid the described issues, the typical solution for LiDAR measurements consists in adopting a gated approach, by switching on the detector only after the internal reflections peak.[47] This approach radically avoids the presence of the first peak, yet at the expenses of a more complex system operation. As demonstrated by our experimental results (see Fig. 7), an alternative and more effective approach relies on the application of the proposed pile-up free method, by using a matched dead time of 50 ns, thus correctly reproducing the whole impinging light waveform even at high rates. We can therefore conclude that the implemented methodology, besides being beneficial in bistatic setups, is also highly suitable in case of monostatic configurations featuring unwanted reflections.

## B. Depth imaging

After carrying out the analysis and characterization of single-point histograms, the remainder of our measurements focused on depth imaging using the monostatic transceiver to faster scan the area of interest. As previously mentioned, two different targets were used: a three-pillar target with known depth features and a more complex pipe model, both spray painted with a black low-reflecting coating. The photographs of the two targets are shown in Fig. 3(c). For each target, two reference depth images were acquired with a long acquisition time of 1 s per pixel, and successively low-rate and high-rate measurements were carried out with a shorter and more realistic acquisition time in the range of 10–30 ms per pixel. In particular, we wanted to compare the situation of matched dead time to the one where the target is situated in correspondence of the blind spot. Afterward, the data analysis consisted in the depth image reconstruction by means of a pixelwise cross correlation between each pixel waveform and the instrument response function (IRF). The IRF consisted in a single-pixel measurement with an acquisition time of 1 s, when using a flat Lambertian reference target with 99% reflectivity (Spectralon, by Labsphere). The cross correlation approach was previously adopted in single-photon LiDAR,[4,13] in order to obtain the delay between the histogram recorded and the IRF, thus obtaining the desired depth map. In particular, the obtained depth values represent the relative distance between the target and the Spectralon position during IRF measurement.

### 1. Pillar target

In Table II, a summary of the measurement parameters employed with the pillar target is reported, subdivided in four different acquisition sets corresponding to reference, low-rate, high-rate,

**TABLE II.** Acquisition parameters for depth imaging of the pillar and the pipe targets. $P_{rec}$ represents the average number of photons recorded by the detector per period.

| Set | $P_{\text{rec}}$ (counts) | Rate (Mcps) | Dead time (ns) | Opt. power (mW) | Env. light | Tissue | Size | Acq. time (s/pix) | Tot. time (s) | Tot. counts (counts/pix) | Pixel loss (%) |
|---|---|---|---|---|---|---|---|---|---|---|---|
| Pillar target | | | | | | | | | | | |
| 1 | 0.05 | 1 | 80 | 0.113 | No | No | 20 × 20 | 1 | 400 | $10^6$ | ⋯ |
| Reference | 0.05 | 1 | 80 | 0.113 | No | Yes | 20 × 20 | 1 | (6 min) | $10^6$ | ⋯ |
| 2 | 0.05 | 1 | 80 | 0.208 | No | Yes | 20 × 20 | 0.01 | 4 | $10^4$ | 61.5 |
| Low rate | 0.05 | 1 | 23 | 0.208 | No | Yes | 20 × 20 | 0.01 | 4 | $10^4$ | 72.8 |
| 3 | 0.25 | 5 | 50 | 1.5 | No | Yes | 20 × 20 | 0.01 | 4 | $5 \times 10^4$ | 5 |
| High rate | 0.25 | 5 | 23 | 1.5 | No | Yes | 20 × 20 | 0.01 | 4 | $5 \times 10^4$ | 37.3 |
| 4 | 0.25 | 5 | 50 | 1.5 | No | Yes | 50 × 50 | 0.01 | 25 | $5 \times 10^4$ | 5 |
| High res. | 0.25 | 5 | 50 | 1.5 | Yes | Yes | 50 × 50 | 0.01 | 25 | $5 \times 10^4$ | 7.6 |
| Pipe target | | | | | | | | | | | |
| 1 | 0.05 | 1 | 80 | 0.135 | No | No | 50 × 50 | 1 | 2500 | $10^6$ | ⋯ |
| Reference | 0.05 | 1 | 80 | 0.135 | No | Yes | 50 × 50 | 1 | (42 min) | $10^6$ | ⋯ |
| 2 | 0.05 | 1 | 80 | 0.135 | No | Yes | 50 × 50 | 0.3 | 750 | $0.3 \times 10^6$ | ⋯ |
| Low rate | ⋯ | ⋯ | ⋯ | ⋯ | ⋯ | ⋯ | ⋯ | ⋯ | (12.5 min) | ⋯ | ⋯ |
| 3 | 0.33 | 6.6 | 50 | 1.88 | No | Yes | 50 × 50 | 0.3 | 750 | $2 \times 10^6$ | ⋯ |
| High rate | 0.33 | 6.6 | 23 | 1.88 | No | Yes | 50 × 50 | 0.3 | (12.5 min) | $2 \times 10^6$ | ⋯ |

and high-resolution acquisitions. In the same table, also the main performance metrics are reported and, in particular, the overall acquisition time per frame and the percentage of pixels lost due to noise or pile-up phenomena.

First, the reference measurements have been carried out with an average number of recorded photon per period $P_{rec}$ of 0.05, i.e., at a photon rate of 1 Mcps, and with a long dead time of 80 ns, as to avoid significant afterpulsing effects. The scanning acquisition consisted in a 20 × 20 rectangular matrix, with an acquisition time of 1 s per pixel, thus an overall scanning time of ~6 minutes and a total number of recorded photons per pixel equal to $10^6$. This procedure allowed us to obtain the reference depth measurements reported in Fig. 8(a) as depth maps at the top and three-dimensional point clouds at the bottom. Because of the long acquisition time per pixel, the acquired measurements faithfully reconstruct the target surface both in the case of the bare target, and also in the presence of the interposed obscurant tissue. As expected, the obscurant highly attenuates the signal from the target, significantly reducing the SBR; nevertheless,

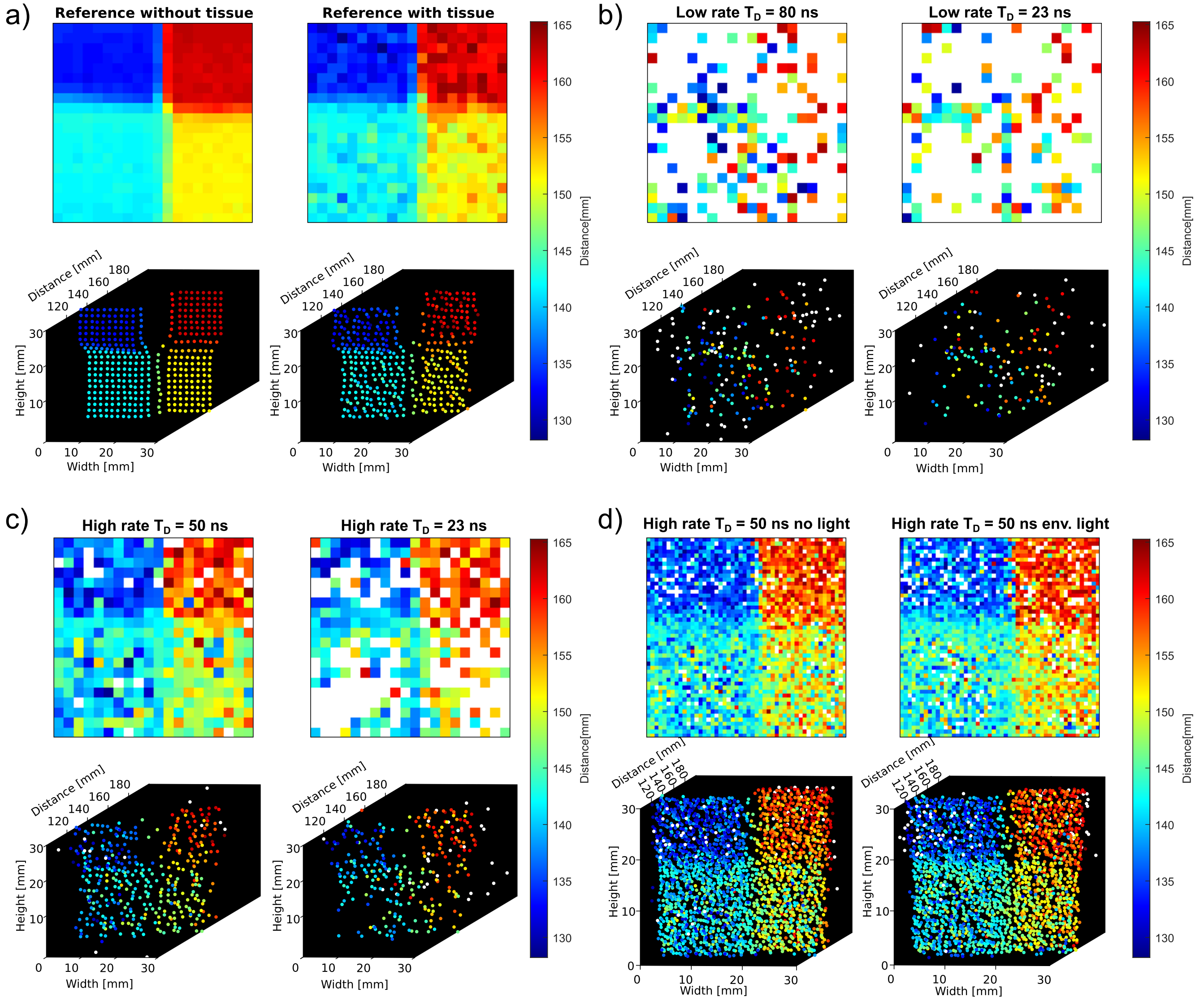

**FIG. 8.** Depth maps (top of each inset) and 3-dimensional point clouds (bottom of each inset) of the three-pillar staircase object in different acquisition conditions (Table II). (a) Low rate ($P_{rec}$ = 0.05) with a long pixel acquisition time (1 s). A comparison is reported between the bare target on the left and the target behind an obscurant on the right. (b) Low rate ($P_{rec}$ = 0.05) with a short pixel acquisition time (10 ms). A comparison is reported between a long dead time of 80 ns on the left and a short dead time of 23 ns on the right (in correspondence of the blind spot). (c) High rate ($P_{rec}$ = 0.25) with a short pixel acquisition time (10 ms). A comparison is reported between a matched dead time of 50 ns on the left and an unmatched dead time of 23 ns on the right (in correspondence of the blind spot). (d) High rate ($P_{rec}$ = 0.25) and high resolution (50 × 50) with a short pixel acquisition time (10 ms). A comparison is reported between a dark environment on the left and the presence of environmental light on the right.

the staircase pillar is still clearly visible, and the distances between the pillars are correctly preserved.

Due to the total scan time for the reference measurement being excessively long, we explored the possibility of reducing the pixel acquisition time to 10 ms, thus achieving a scanning time of 4 s, while still keeping a low rate count rate to avoid pile-up. The results of this second set of measurements are reported in Fig. 8(b) for the target behind the obscurant, and in this case, the pillar target is not recognizable in both the depth map and the point cloud. The main reasons for the target disappearance consist in the low number of total recorded photons per pixel $(10^4)$, in conjunction with the low amplitude of the target peak. In particular, the out-of-scale depth points are reported in white color, for a total percentage of lost pixels equal to 61.5% in case of a long dead time (80 ns). For the sake of completeness, the same measurement was repeated with a dead time of 23 ns, which corresponds to the previously mentioned blind spot (Fig. 7); in this situation, the pixel loss becomes even worse, i.e., equal to 72.8%. Since the additional pixel loss cannot be attributed to pile-up in case of low rates, the increased disturbance might be driven by the higher afterpulsing that is present for lower dead time values.

At this stage, it was consequently evident that a low-rate measurement with a short acquisition time was not a viable option for a correct depth reconstruction, and a high-flux LiDAR was necessary to obtain an adequate depth map. For this reason, the photon rate was increased to 5 Mcps ($P_{rec} = 0.25$), and further depth maps were acquired with a matched dead time of 50 ns (see set 3 in Table II), and with an unmatched dead time of 23 ns, corresponding to the blind spot. The obtained results are illustrated in Fig. 8(c), where the depth map that features a matched dead time exhibits only a 5% pixel loss, thanks to the higher number of integrated photons per pixel $(5 \times 10^4)$. Instead, despite possessing the same number of counts per pixel, the map with unmatched dead time shows a 37.3% pixel loss (six times higher) due to the return peak from the target being covered by the distortions in the histogram. This result clearly validates the usage of high-flux LiDAR in conjunction with the proposed pile-up free methodology for the correct surface reconstruction of a target behind an obscurant. To further confirm the achieved results, we performed a last set of measurements with matched dead time and an increased spatial resolution of 50 × 50, still with a 10 ms integration time per pixel, i.e., with an overall acquisition time of 25 s. Figure 8(d) shows the obtained results with a similar 5% pixel loss in case of a dark environment, and with a negligible increase up to 7.6% in the presence of environmental light (background photon rate equal to 70 kcps on the detector).

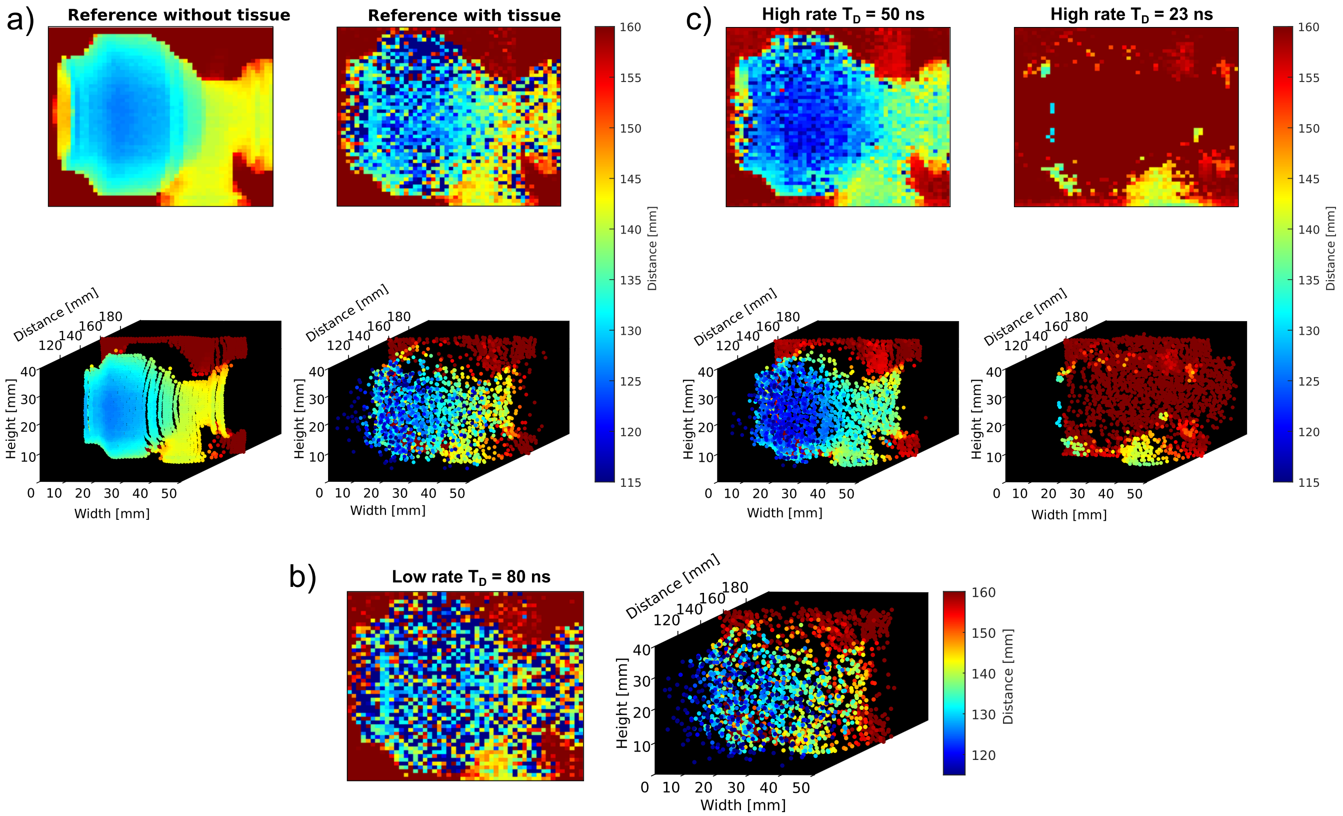

**FIG. 9.** Depth maps and three-dimensional point clouds of the pipe surface under different acquisition conditions (Table II). (a) Low rate ($P_{rec}$ = 0.05) with a long pixel acquisition time (1 s). A comparison is reported between the bare target on the left and the target behind an obscurant on the right. (b) Low rate ($P_{rec}$ = 0.05) with a short pixel acquisition time (300 ms). (c) High rate ($P_{rec}$ = 0.33) with a short pixel acquisition time (300 ms). A comparison is reported between a matched dead time of 50 ns on the left and an unmatched dead time of 23 ns on the right (in correspondence of the blind spot).

Finally, it is worth mentioning that—ideally—the image quality may be improved by applying post-processing filters, which reduce the noise over-imposed to the images. However, by using a simple median filter applied to the previous depth maps, the pixel loss appears to drastically reduce below 1% in the case of a matched dead time, while it is only slightly decreased to 30% in the specific case of the blind spot. This further strengthens the necessity of a proper acquisition methodology to avoid pile-up in case of high-flux LiDAR with low reflectivity targets behind obscurants.

### *2. Pipe target*

As a final depth measurement, we imaged a small pipe joint, in order to validate the methodology on a more complex surface that better resembles a real-world object. In Table II, the main parameters and performance metrics for three different sets of measurements (reference, low count rate, and high count rate) are reported. For these measurements, a scanning matrix of 50 × 50 pixels was selected due to the higher complexity of the target under test and the bigger field of view needed.

First, a reference depth map both with and without the tissue was acquired at low rate ($P_{rec} = 0.05$, i.e., 1 Mcps) with a pixel acquisition time of 1 s, a number of photons per pixel equal to $10^6$, and an overall scanning time of 42 min. The obtained images can be observed in Fig. 9(a), where the presence of the tissue worsens the depth image of the target. Successively, with the aim of reducing the acquisition time without incurring in pile-up, we performed a low count rate acquisition with a pixel integration time of 300 ms, which corresponds to $0.3 \times 10^6$ total counts per pixel and to an overall scanning time of 12.5 min. As already observed in Sec. III B 1, the acquired depth map [Fig. 9(b)] results unreliable, being the specific pipe features not clearly visible. Following the same approach as for the three-pillar object, the count rate was increased to 6.6 Mcps ($P_{rec} = 0.33$) and the experiment was repeated for matched (50 ns) and unmatched (23 ns) dead times; in this case, the total number of photons per pixel results equal to $2 \times 10^6$. Figure 9(c) shows the final results: for the matched dead time, the image is reconstructed with a satisfactory level of detail, while for the unmatched dead time, the pipe surface is no longer recognizable.

In conclusion, also the final measurements with the pipe target confirm the possibility to successfully apply the considered pile-up free methodology to LiDAR waveforms in case of high-flux stimulation, both with single-point ranging and with depth imaging. This procedure allows, indeed, to enhance the measurement speed while avoiding pile-up distortion. Moreover, it is worth observing that the total acquisition time may further benefit from a remarkable reduction in the case of faster excitation lasers.

## IV. DISCUSSION AND METHOD COMPARISON

In the previous sections, we have explored a variety of possible pile-up effects on LiDAR through obscurants at high photon fluxes, both in the simpler case of single-point ranging and in depth-imaging. Although most scientific literature on the topic only refers to possible peak displacements at high rates,[20,25] we clearly showed—by means of original data—that other detrimental effects appear above the 5% pile-up limit, and in particular,

- the whole waveform can be easily distorted due to fictitious baseline shifts and steps, leading to additional or missing feature identification in the waveform analysis;
- the peak amplitudes and their relative ratios can be affected by the presence of such non-ideal features, with potential consequences on reflectivity estimation; and
- under specific circumstances, the presence of the target peak can be hidden by the distorted waveform, giving origin to spatial blind spots and unrecognized targets.

To overcome these issues, we proposed to apply a hardware methodology based on dead time matching. While the method proves to be effective in removing the undesired pile-up distortions, it is worth comparing its practical application to the current software approaches, as the ones proposed by Rapp *et al.*,[24,25] Isbaner *et al.*,[23] and Rech *et al.*[37] Indeed, a radically different method to register LiDAR curves would be to shorten the detector dead time to its lowest value and to apply a software correction to the acquired waveforms. This solution allows registering a higher number of photons, thanks to the shorter dead time, at the expense of a systematic curve masking after the obscurant peak (as in Figs. 4 and 7 with 13 ns dead time). Consequently, the trade-offs between the different alternatives are not immediately evident and must be carefully assessed. It should be emphasized that a direct comparison with the other software-based approaches discussed in Sec. I—namely those proposed by Heide *et al.*[20] and Tontini *et al.*[21]—would not be meaningful, as their correction strategies rely on synchronous acquisition schemes, which are not representative of the free-running detector configuration considered in this work.

In Fig. 10, we report an illustrative comparison between a histogram acquired with the matched dead time of 50 ns and software-corrected histograms (with Rech *et al.*[37] and Rapp *et al.*[24] methods) acquired with the lowest possible dead time of 13 ns, both in the case of bistatic setup. Conversely, a histogram corrected with Isbaner *et al.*[23] approach has not been reported in the figure because this method appears ineffective in correcting the baseline downshift induced by the pile-up, as already shown in Ref. 25 and verified in the supplementary material. The original data in Fig. 10 are the same of Fig. 4, reported here without any normalization for a clearer comparison. Specific details on the correction implementation are described in the supplementary material. As can be observed, the software corrections allow for an effective retrieval of the histogram baseline, with the resulting histograms from the two software methods exhibiting an almost perfect overlap. To better compare the hardware and software corrections, we evaluated the signal-to-noise (SNR) ratio in correspondence of the target peak, resulting in 12.9 for the corrected curves with 13 ns dead time and 10.2 for the curve at 50 ns. Despite the higher number of photons collected with the shorter dead time, the SNR is comparable in the two cases. However, a shorter dead time results in a higher afterpulsing,[45] and in increased ringings over the waveform; moreover, the onset of afterpulsing is placed in this case in the range of interest, and can therefore hide an overlapping target peak. Instead, in case of matched (and longer) dead time, the afterpulsing is lower, and its onset is situated in correspondence of the obscurant peak, hence significantly lowering its impact on the target peak.

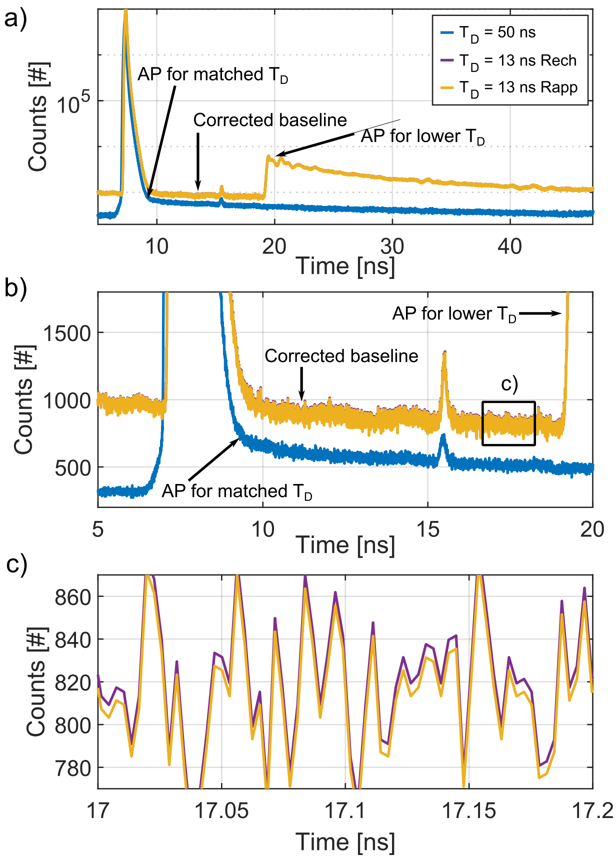

**FIG. 10.** Comparison between dead-time matching technique and alternative software corrections, based on Rech *et al.*[37] and Rapp *et al.*[24] methods, with a constant acquisition time. The data are reported without normalization, and the legend is valid for all graphics. AP: afterpulsing, $T_D$: dead time. (a) Full histograms with (i) dead time of 50 ns and (ii) and (iii) dead time of 13 ns, including the software corrections. The two software corrected histograms appear indistinguishable due to an almost perfect overlap. (b) Zoom on linear scale in correspondence of the histogram region of interest. (c) Zoom on linear scale in correspondence of the baseline [see the rectangle in the inset (b)], showing the almost overlapped software-corrected curves.

In summary, even if the presented quantitative results are related to the employed detector, the considerations can apply on a more general scale, thus outlining the possible benefits of the proposed hardware technique. A full investigation of the conditions under which one method may be preferable over the others in practical scenarios will be the subject of future work. To our opinion, one possible current limitation of the discussed hardware technique is the lack of commercial SPAD modules featuring tunable dead time. However, being the detector dead time typically controlled by an AQC,[42] we expect that custom modules can be easily available upon request from manufacturers, or that standard SPAD modules may be directly modified to achieve dead time regulation, as shown, for instance, in Ref. 48. Finally, we believe that the proposed technique is directly scalable to multi-channel LiDAR systems, provided that an integrated multi-channel AQC is designed with a tunable dead time. Depending on the dead time mismatch between the different AQC channels, a single voltage signal $V_Q$ may be used to control the whole array, or fully separated dead time control circuits may be implemented. Moreover, we believe that the technique is transferrable to other detector technologies and implementations (e.g., SPADs based on CMOS[27]).

## V. CONCLUSION

In this work, we have extensively addressed the effects of pile-up on single-photon LiDAR for imaging through obscurants. Starting from numerical simulations, we have assessed the main waveform distortions, which have been later observed both in single-point measurements and in depth imaging. Moreover, we have applied for the first time to single-photon LiDAR a hardware-based method that overcomes pile-up limitations, by matching the detector dead time to the laser period. We have demonstrated that the method not only prevents pile-up distortions directly at acquisition, but it also offers several advantages over software-based corrections: (i) it enables real-time acquisition, as no post-processing time is needed for histogram correction and (ii) it potentially reduces system complexity, as it requires only a single detector with matched dead time. Furthermore, despite collecting a lower number of photon events, the method achieves a similar SNR when compared to software corrections, and it mitigates possible issues generated by the detector afterpulsing.

These results demonstrate that the proposed strategy enables significant improvements in LiDAR systems operating at high flux and high speed. We anticipate particular benefits for imaging through obscurants, underwater imaging, and hyperspectral and multispectral imaging.

## SUPPLEMENTARY MATERIAL

See the supplementary material for additional information on the simulation of pile-up effects, on the experimental setups and parameters, and on the comparison between the proposed hardware method and software corrections.

## ACKNOWLEDGMENTS

This work was funded by the Royal Academy of Engineering under the Research Fellowship scheme (No. RF\201920\19\190) and Ministero dell'Università e della Ricerca under the PRIN scheme (No. 2022NEJZ2C). The authors acknowledge the support of UK Engineering and physical Science Research Council Project Nos. EP/T00097X/1 and EP/S026428/1.

The authors gratefully thank Dr. Joshua Rapp for providing the code employed in the comparisons.

## AUTHOR DECLARATIONS

### Conflict of Interest

The authors have no conflicts to disclose.

### Author Contributions

**Serena Farina**: Conceptualization (equal); Investigation (equal); Methodology (equal); Visualization (lead); Writing – original draft (lead); Writing – review & editing (lead). **Aurora Maccarone**: Conceptualization (equal); Funding acquisition (equal); Investigation (equal); Methodology (equal); Writing – original draft (supporting); Writing – review & editing (equal). **Ivan Labanca**: Resources (equal). **Aongus McCarthy**: Resources (equal); Writing – review & editing (equal). **Giulia Acconcia**: Funding acquisition (equal); Writing – review & editing (equal). **Ivan Rech**: Conceptualization (supporting); Methodology (supporting); Supervision (equal); Writing – review & editing (equal). **Gerald S. Buller**: Conceptualization (supporting); Funding acquisition (equal); Methodology (supporting); Supervision (equal); Writing – review & editing (equal).

## DATA AVAILABILITY

The data that support the findings of this study are available from the corresponding author upon reasonable request.

## REFERENCES

[1] U. Wandinger, "Introduction to LiDAR," in *LiDAR: Range-Resolved Optical Remote Sensing of the Atmosphere* (Springer, 2005), pp. 1–18.

[2] C. Fernández, M. Gavilán, D. F. Llorca, I. Parra, R. Quintero, A. G. Lorente, L. Vlacic, and M. Sotelo, "Free space and speed humps detection using LiDAR and vision for urban autonomous navigation," in *2012 IEEE Intelligent Vehicles Symposium* (IEEE, 2012), pp. 698–703.

[3] Y. Li and J. Ibanez-Guzman, "LiDAR for autonomous driving: The principles, challenges, and trends for automotive LiDAR and perception systems," IEEE Signal Process. Mag. **37**, 50–61 (2020).

[4] A. Maccarone *et al.*, "Underwater depth imaging using time-correlated single-photon counting," Opt. Express **23**, 33911–33926 (2015).

[5] A. Maccarone, K. Drummond, A. McCarthy, U. K. Steinlehner, J. Tachella, D. A. Garcia, A. Pawlikowska, R. A. Lamb, R. K. Henderson, S. McLaughlin *et al.*, "Submerged single-photon LiDAR imaging sensor used for real-time 3D scene reconstruction in scattering underwater environments," Opt. Express **31**, 16690–16708 (2023).

[6] W. Chen, P. Chen, H. Zhang, Y. He, J. Tang, and S. Wu, "Review of airborne Oceanic LiDAR remote sensing," Intell. Mar. Technol. Syst. **1**, 10 (2023).

[7] S. Rijal, G. Wang, P. B. Woodford, H. R. Howard, J. M. S. Hutchinson, S. Hutchinson, J. Schoof, T. J. Oyana, R. Li, and L. O. Park, "Detection of gullies in fort riley military installation using LiDAR derived high resolution DEM," J. Terramech. **77**, 15–22 (2018).

[8] A. M. Wallace, A. Halimi, and G. S. Buller, "Full waveform LiDAR for adverse weather conditions," IEEE Trans. Veh. Technol. **69**, 7064–7077 (2020).

[9] R. H. Hadfield, J. Leach, F. Fleming, D. J. Paul, C. H. Tan, J. S. Ng, R. K. Henderson, and G. S. Buller, "Single-photon detection for long-range imaging and sensing," Optica **10**, 1124–1141 (2023).

[10] W. Becker, *Advanced Time-Correlated Single Photon Counting Techniques* (Springer, 2005).

[11] S. Farina, I. Labanca, G. Acconcia, and I. Rech, "A 4.5 ps precision TCSPC system: Design principles and characterization," IEEE J. Sel. Top. Quantum Electron. **30**, 1 (2024).

[12] C. Pei, H. Li, X. Zeng, Y. Wang, H. Chen, and D. D.-U. Li, "Multi-channel high-precision FPGA-embedded time correlated single photon counting systems for optical scattering imaging," Opt. Express **33**, 46626–46641 (2025).

[13] R. Tobin, A. Halimi, A. McCarthy, M. Laurenzis, F. Christnacher, and G. S. Buller, "Three-dimensional single-photon imaging through obscurants," Opt. Express **27**, 4590–4611 (2019).

[14] N. C. Coops, P. Tompalski, T. R. H. Goodbody, M. Queinnec, J. E. Luther, D. K. Bolton, J. C. White, M. A. Wulder, O. R. van Lier, and T. Hermosilla, "Modelling LiDAR-derived estimates of forest attributes over space and time: A review of approaches and future trends," Remote Sens. Environ. **260**, 112477 (2021).

[15] P.-Y. Jiang, Z.-P. Li, W.-L. Ye, Y. Hong, C. Dai, X. Huang, S.-Q. Xi, J. Lu, D.-J. Cui, Y. Cao *et al.*, "Long range 3D imaging through atmospheric obscurants using array-based single-photon LiDAR," Opt. Express **31**, 16054–16066 (2023).

[16] R. Kitichotkul, J. Rapp, and V. K. Goyal, "The role of detection times in reflectivity estimation with single-photon LiDAR," IEEE J. Sel. Top. Quantum Electron. **30**, 1 (2024).

[17] Y. Chen, C. Jiang, J. Hyyppä, S. Qiu, Z. Wang, M. Tian, W. Li, E. Puttonen, H. Zhou, Z. Feng *et al.*, "Feasibility study of ore classification using active hyperspectral LiDAR," IEEE Geosci. Remote Sens. Lett. **15**, 1785–1789 (2018).

[18] B. Wang, J. Liu, J. Li, and M. Li, "UAV LiDAR and hyperspectral data synergy for tree species classification in the Maoershan forest farm region," Remote Sens. **15**, 1000 (2023).

[19] P. B. Coates, "The correction for photon 'pile-up' in the measurement of radiative lifetimes," J. Phys. E: Sci. Instrum. **1**, 878 (1968).

[20] F. Heide, S. Diamond, D. B. Lindell, and G. Wetzstein, "Sub-picosecond photon-efficient 3D imaging using single-photon sensors," Sci. Rep. **8**, 17726 (2018).

[21] A. Tontini, S. Mazzucchi, R. Passerone, and L. Gasparini, "A post-processing histogram compensation method for SPAD-based d-ToF LiDAR systems for high photon flux measurements," IEEE Access **12**, 135390 (2024).

[22] J. Arlt, D. Tyndall, B. R. Rae, D. D.-U. Li, J. A. Richardson, and R. K. Henderson, "A study of pile-up in integrated time-correlated single photon counting systems," Rev. Sci. Instrum. **84**, 103105 (2013).

[23] S. Isbaner, N. Karedla, D. Ruhlandt, S. C. Stein, A. Chizhik, I. Gregor, and J. Enderlein, "Dead-time correction of fluorescence lifetime measurements and fluorescence lifetime imaging," Opt. Express **24**, 9429–9445 (2016).

[24] J. Rapp, Y. Ma, R. M. A. Dawson, and V. K. Goyal, "Dead time compensation for high-flux ranging," IEEE Trans. Signal Process. **67**, 3471–3486 (2019).

[25] J. Rapp, Y. Ma, R. M. A. Dawson, and V. K. Goyal, "High-flux single-photon LiDAR," Optica **8**, 30–39 (2021).

[26] A. Incoronato, M. Locatelli, and F. Zappa, "Statistical modelling of SPADs for time-of-flight LiDAR," Sensors **21**, 4481 (2021).

[27] F. Severini, I. Cusini, D. Berretta, K. Pasquinelli, A. Incoronato, and F. Villa, "Spad pixel with sub-ns dead-time for high-count rate applications," IEEE J. Sel. Top. Quantum Electron. **28**, 1–8 (2022).

[28] F. Gramuglia, M.-L. Wu, C. Bruschini, M.-J. Lee, and E. Charbon, "A low-noise CMOS SPAD pixel with 12.1 ps SPTR and 3 ns dead time," IEEE J. Sel. Top. Quantum Electron. **28**, 1–9 (2022).

[29] PicoQuant, rapidflimhires, https://www.picoquant.com/rapidFLIM#paper, accessed February 29, 2024.

[30] A. Incoronato, I. Cusini, K. Pasquinelli, and F. Zappa, "Single-shot pulsed-LiDAR SPAD sensor with on-chip peak detection for background rejection," IEEE J. Sel. Top. Quantum Electron. **28**, 1–10 (2022).

[31] A. Gupta, A. Ingle, A. Velten, and M. Gupta, "Photon-flooded single-photon 3D cameras," in *Proceedings of the IEEE/CVF Conference on Computer Vision and Pattern Recognition* (IEEE, 2019), pp. 6770–6779.

[32] A. Gupta, A. Ingle, and M. Gupta, "Asynchronous single-photon 3D imaging," in *Proceedings of the IEEE/CVF International Conference on Computer Vision* (IEEE, 2019), pp. 7909–7918.

[33] A. Tontini, S. Mazzucchi, R. Passerone, N. Broseghini, and L. Gasparini, "Histogram-less LiDAR through SPAD response linearization," IEEE Sens. J. **24**, 4656–4669 (2024).

[34] PicoQuant, Multiharp 150, https://www.picoquant.com/products/category/tcspc-and-time-tagging-modules/multiharp-150-high-throughput-multichannel-event-timer-tcspc-unit , accessed February 29, 2024.

[35] F. Malanga, G. Acconcia, S. Farina, M. Ghioni, and I. Rech, "Versatile multichannel time-to-amplitude converter for high-speed and high-precision timing applications," Proc. SPIE **PC12089**, PC120890C (2022).

[36] A. Cominelli, G. Acconcia, P. Peronio, M. Ghioni, and I. Rech, "High-speed and low-distortion solution for time-correlated single photon counting measurements: A theoretical analysis," Rev. Sci. Instrum. **88**, 123701 (2017).

[37] I. Rech, A. Bovolenta, A. Cominelli, and G. Acconcia, "Toward constraintless time-correlated single-photon counting measurements: A new method to remove pile-up distortion," IEEE J. Sel. Top. Quantum Electron. **30**, 1–12 (2024).

[38] S. Farina, I. Labanca, G. Acconcia, A. Ghezzi, A. Farina, C. D'Andrea, and I. Rech, "Above pile-up fluorescence microscopy with a 32 Mc/s single-channel time-resolved spad system," Opt. Lett. **47**, 82–85 (2022).

[39]S. Instruments, Time tagger ultra, https://www.swabianinstruments.com/time-tagger, accessed February 29, 2024.

[40]S. Farina, G. Acconcia, I. Labanca, M. Ghioni, and I. Rech, "Toward ultra-fast time-correlated single-photon counting: A compact module to surpass the pile-up limit," Rev. Sci. Instrum. **92**, 063702 (2021).

[41]S. Pellegrini, G. S. Buller, J. M. Smith, A. M. Wallace, and S. Cova, "Laser-based distance measurement using picosecond resolution time-correlated single-photon counting," Meas. Sci. Technol. **11**, 712 (2000).

[42]G. Acconcia, I. Rech, A. Gulinatti, and M. Ghioni, "High-voltage integrated active quenching circuit for single photon count rate up to 80 Mcounts/s," Opt. Express **24**, 17819–17831 (2016).

[43]S. Farina, A. Ghezzi, I. Labanca, G. Acconcia, C. D'Andrea, A. Farina, and I. Rech, "Pile-up free fluorescence lifetime imaging with a SPAD-based single pixel camera," Opt. Express **33**, 22296–22307 (2025).

[44]M. Ghioni, A. Gulinatti, I. Rech, F. Zappa, and S. Cova, "Progress in silicon single-photon avalanche diodes," IEEE J. Sel. Top. Quantum Electron. **13**, 852–862 (2007).

[45]A. Giudice, M. Ghioni, S. Cova, and F. Zappa, "A process and deep level evaluation tool: Afterpulsing in avalanche junctions," in *ESSDERC'03. 33rd Conference on European Solid-State Device Research, 2003* (IEEE, 2003), pp. 347–350.

[46]S. Cova, A. Lacaita, and G. Ripamonti, "Trapping phenomena in avalanche photodiodes on nanosecond scale," IEEE Electron Device Lett. **12**, 685–687 (1991).

[47]A. McCarthy, R. J. Collins, N. J. Krichel, V. Fernández, A. M. Wallace, and G. S. Buller, "Long-range time-of-flight scanning sensor based on high-speed time-correlated single-photon counting," Appl. Opt. **48**, 6241–6251 (2009).

[48]S. Farina, I. Labanca, G. Acconcia, M. Ghioni, and I. Rech, "10-nanosecond dead time and low afterpulsing with a free-running reach-through single-photon avalanche diode," Rev. Sci. Instrum. **93**, 053102 (2022).